actuators

MDPI

Article

Modeling and Clamping Force Tracking Control of an Integrated Electric Parking Brake System Using Sliding-Mode-Based Observer

Jiawang Yong [1,*], Liang Li [2], Dongliang Wang [3] and Yahui Liu [2]

[1] Department of Traffic Engineering, Beijing University of Technology, Beijing 100124, China
[2] State Key Laboratory of Automotive Safety and Energy, Tsinghua University, Beijing 100084, China; liangl@tsinghua.edu.cn (L.L.); liuyahui@tsinghua.edu.cn (Y.L.)
[3] Trinova-Tech Co., Ltd., Tianjin 301701, China; wangdl1993@163.com
* Correspondence: yongjw@bjut.edu.cn; Tel.: +86-18810800229

Abstract: This article proposes a hierarchical control strategy to address semi-ABS control as well as the precise clamping force control problems for an integrated electric parking brake (iEPB) system. To this end, a detailed system model, including modeling of the motor, transmission mechanism, friction and braking torque, is constructed for controller and observer design, and a sliding-mode-based observer (SMO) is proposed to estimate the load torque by using the motor rotational speed without installing a force sensor. In addition, a stable and reliable tire–road friction coefficient (TRFC) estimation method is adopted, and the desired slip ratio (DSR) is observed as the target that the rear wheels cycle around. At the upper level of the hierarchical control structure, the desired clamping forces of the rear wheels are generated using a sliding mode control (SMC) technique, and the control objective is to track the DSR to make full use of the road condition. At the lower level, the motor is controlled to track the desired clamping force generated from the upper controller. The hardware-in-the-loop (HIL) experimental results demonstrate the effectiveness and high tracking precision of the proposed strategy under different road conditions, and the estimation parameters based on the proposed observers are timely and accurate to satisfy the control requirements.

Keywords: integrated electric parking brake; sliding-mode control; sliding-mode-based observer; parameter estimation; anti-lock brake control

check for updates

Citation: Yong, J.; Li, L.; Wang, D.; Liu, Y. Modeling and Clamping Force Tracking Control of an Integrated Electric Parking Brake System Using Sliding-Mode-Based Observer. *Actuators* **2024**, *13*, 39. https://doi.org/10.3390/act13010039

Academic Editor: Keigo Watanabe

Received: 3 December 2023
Revised: 12 January 2024
Accepted: 12 January 2024
Published: 17 January 2024

Copyright: © 2024 by the authors. Licensee MDPI, Basel, Switzerland. This article is an open access article distributed under the terms and conditions of the Creative Commons Attribution (CC BY) license (https://creativecommons.org/licenses/by/4.0/).

1. Introduction

An iEPB system achieves better performance in terms of its fast response and active function in contrast to traditional parking brake systems [1,2], and it will dominate the parking brake market in the future. In addition to the parking brake function, an iEPB system could also implement a secondary braking function if the primary braking system fails, or it could realize active safety functions by regulating the clamping forces. However, for active safety function applications, the regulation of the clamping forces will cause a risk of the vehicle spinning if the iEPB is applied without slip ratio control, especially on low-adhesion-coefficient surfaces. Therefore, to ensure the vehicle stability during conditions with an applied active safety function, the slip ratio of iEPB-equipped wheels should be controlled precisely and steadily to track the DSR based on the vehicle's system dynamics [3,4].

The slip ratio reveals the maximum adhesion forces that the road can provide, both in the longitudinal and lateral directions, and it is also adopted as an indicator of the wheel-locking status. Many methods have been proposed to address the slip ratio control problem [4–8], and the algorithms should normally have two features: (1) an optimal slip ratio should firstly be estimated with different road conditions, and (2) a controller should be designed to control the slip ratio following the optimal one for improving the stability

and security performance of the vehicle during acceleration/braking situations. Note that the TRFC is critical in determining the optimal slip ratio, so a high-precision TRFC observer should be first developed. Although the accuracy of these TRFC observers [9–11] has been verified by simulations and experiments, they are too complex, and the associated complicated computation requirements will significantly decrease the executing efficiency of the micro-controller chip (MCU) integrated in the vehicle's electric control unit (ECU). Hence, a practical and effective observer should be proposed that can be properly utilized in practical control situations with a low-cost MCU.

The control of a direct-current (DC) motor is complicated because of the presence of disturbances, measurement noise and load torque perturbations, which have promoted research into observer-based sensorless control. Ref. [12] presented a new extended nonlinear approach to estimate the motor speed and load torque simultaneously, and an augmented dynamical system was created by affiliating a supplementary dynamic into the motor model to admit changes in coordinates. However, the performance of the method depends on the model's accuracy and system parameters. Sliding-mode-based methods and observers have been studied in recent years, and they benefit from their insensitivity to parameter variations and disturbances [13–15]. Ref. [16] regarded system inertia and friction and designed an SMC-based load torque estimation method. Ref. [17] proposed a motor speed and torque observer with consideration of electrical and mechanical parameter disturbances and the voltage reconstruction error as well. To eliminate the chattering problem, ref. [18] deduced and analyzed the mathematical model of a traditional SMC-based load torque identification observer, and a new one was designed by employing a saturation function instead of the sign one. However, this method requires an offline table, which is generated from experimental results, for parameter optimization and disturbance compensation, and this will limit the identification accuracy, especially in high-speed conditions. Some other studies into the load torque estimation of different actuators are also helpful for motor load torque observation [19–21].

With the above observers, an iEPB system should be quickly and precisely operated over a wide range of clamping forces to meet the requirements, whether from the driver or from the upper controllers as a brake-by-wire system. Ref. [22] proposed a nonlinear proportional clamping force controller for an electric parking system using the measured clamping force to improve the control performance based on a state-independent switched system model. However, it is too expensive to install an embedded clamping force sensor in production vehicles, and the measurement accuracy at high temperatures is also a worrying aspect. To solve these problems, observers should seek to estimate the clamping force without measurement sensors. Ref. [23] estimated the clamping force through the angular displacement of a DC motor and approximated the initial contact point using the motor angular velocity to prevent the error caused by the gap between the brake pad and disk at release, whereas the estimation precision was affected by the age and temperature of the contact point. In [24,25], the clamping force control methods used for an electromechanical brake system are studied, and these could also be applicable for an iEPB after a few modifications.

The above studies have acquired many achievements in improving the control performance of iEPB systems. However, it is still a big challenge to comprehensively and precisely control the clamping force of an iEPB to realize active braking functions. In this paper, a hierarchical control strategy to address semi-ABS control as well as the precise clamping force control problems for an iEPB system are proposed, which provide the potential for iEPB systems to be applied in active braking control or even in implementing a secondary braking function if the primary braking system fails. To this end, an eight-degrees-of-freedom nonlinear vehicle model, a tire model and a detailed iEPB system model are established for controller design and parameter observation. Meanwhile, a stable and reliable TRFC observation method is adopted to estimate the TRFC and DSR, and an SMO is proposed to estimate the load torque by using the motor rotational speed without installing a force sensor. Furthermore, a hierarchical control structure, which contains an upper controller

to track the DSR to realize semi-ABS function and a lower controller to track the desired clamping force based on the SMO, is designed. Finally, numerical experiments are carried out on an HIL test bench to evaluate the proposed algorithm.

The rest of the paper is organized as follows: in Section 2, the involved models are established, including a vehicle model, a tire model and an iEPB system model. An SMC-based observer for motor load torque estimation is presented in Section 3. Section 4 describes the semi-ABS and clamping force control strategies. HIL experimental results are presented to discuss the performance of the proposed algorithm in Section 5. Conclusions are given in the end.

2. System Modeling

In this section, an eight-degrees-of-freedom (8-DOF) nonlinear vehicle model and tire model are presented for simulation and parameter estimation; a control-oriented iEPB system model, including a DC motor model, a transmission mechanism model, a brake model, a screw-nut model and a caliper model, is proposed for controller design.

2.1. Vehicle Model

The governing equations of motions of the sprung mass can be expressed as shown below [26,27]:

$$m(\dot{u} - rv_a) - m_\varphi h_\varphi(\varphi\dot{r} + 2r\dot{\varphi}) = Q_u \tag{1}$$

$$m(\dot{v}_a + ru) + m_\varphi h_\varphi(\ddot{\varphi} - r^2\varphi) = Q_v \tag{2}$$

$$I_z\dot{r} + I_{z\varphi}\theta_r\ddot{\varphi} - m_\varphi h_\varphi(\ddot{u} - rv_a)\varphi = Q_r \tag{3}$$

$$(I_{x\varphi} + m_\varphi h_\varphi^2)\ddot{\varphi} + m_\varphi h_\varphi(\dot{v}_a + ru) + I_z\theta_r\dot{r} - (m_\varphi h_\varphi^2 + I_{y\varphi} - I_{z\varphi})r^2\varphi + (C_\varphi - m_\varphi g h_\varphi)\varphi = Q_\varphi \tag{4}$$

where m represents the vehicle mass. u and v_a stand for the longitudinal and lateral velocities, respectively. r denotes the yaw rate. m_φ is the vehicle sprung mass. h_φ stands for the height of the center of roll part gravity with respect to (WRT) the roll axis. φ denotes the roll angle around the roll axis. θ_r indicates the inclination angle of the roll axis WRT horizontal plane. C_φ describes the total roll stiffness. I_z represents the yaw moment of inertia around the z-axis. $I_{x\varphi}$, $\mathrm{I}_{y\varphi}$ and $I_{z\varphi}$ stand for the rotational inertias of sprung mass around the x-axis, y-axis and z-axis, respectively. Q_u, Q_r, $Q_\varphi$and Q_v represent the general forces of the x-axis, y-axis, yaw motion and roll motion, respectively.

$$Q_u = m\dot{u} = (F_{x11} + F_{x12})cos(\delta) + F_{x21} + F_{x22} - (F_{y11} + F_{y12})sin(\delta) + mrv_a \tag{5}$$

$$Q_v = m\dot{v}_a = F_{y21} + F_{y22} + (F_{f11} + F_{x12})sin(\delta) \ + (F_{y11} + F_{y12})cos(\delta) - mru \tag{6}$$

$$\begin{aligned} Q_r = I_z\dot{r} = \ & a(F_{x11} + F_{x12})sin(\delta) + a(F_{y11} + F_{y12})cos(\delta) - b(F_{y21} + F_{y22}) \\ & + \tfrac{t_w}{2}(F_{x12} - F_{x11})cos(\delta) + \tfrac{t_w}{2}(F_{x22} - F_{x21}) + \tfrac{t_w}{2}(F_{y11} - F_{y12})sin(\delta) \end{aligned} \tag{7}$$

$$Q_\varphi = (k_{\varphi1} + k_{\varphi2})\dot{\varphi} \tag{8}$$

where F expresses the tire forces, the subscripts x and y indicate the x-axis and y-axis, respectively, and the subscripts 11, 12, 21 and 22 denote the front-left, front-right, rear-left and rear-right wheel; accordingly, these subscripts represent the same definition in the following appearance. Δ is the total applied steer angle, t_w is the wheel track, and a and b are the horizontal distances from the center of gravity to the front and rear axles, respectively. $k_{\varphi1}$ and $k_{\varphi2}$ represent the roll damping coefficients of the front and rear axles, respectively.

The vertical load transfer occurs during acceleration or deceleration situations, and is can be expressed as follows

$$F_{zij} = F_{zsij} \pm \frac{h_g m\dot{u}}{2L} \pm \frac{h_g m\dot{v}_a}{2t_w} \tag{9}$$

in which F_z and F_{zs} indicate the vertical dynamic and static forces on wheels, L denotes the wheelbase, ij represents 11, 12, 21, and 22. In addition, + and − need to be properly selected for different wheels. It is assumed that the lateral inertia force is located on four wheels equally in this paper.

The rotational motions of wheels are as follows:

$$\begin{cases} J_f\dot{\omega}_{11} = T_{w11} - f_{x11}R_f - T_{b11} \\ J_f\dot{\omega}_{12} = T_{w12} - f_{x12}R_f - T_{b12} \\ J_r\dot{\omega}_{21} = f_{x21}R_r - T_{b21} - T_{epb21} \\ J_r\dot{\omega}_{22} = f_{x22}R_r - T_{b22} - T_{epb22} \end{cases} \tag{10}$$

in which J_f and J_r denote the rotational inertias of the front and rear wheels, respectively. R_f and R_r are the radiuses of the front and rear wheels, accordingly. T_b is the hydraulic braking torque of different wheels. T_{epb} is the braking torque of rear wheels applied from the iEPB system, and T_w is the driving torque of different wheels.

2.2. Tire Model

The nonlinear Dugoff tire model defines the longitudinal and lateral tire forces as shown below [28]:

$$F_{0x} = C_k \frac{s}{1+|s|} f(\kappa) \tag{11}$$

$$F_{0y} = -C_\alpha \frac{tan(\alpha)}{1+|s|} f(\kappa) \tag{12}$$

In which $C_k = C_s F_z$ represents the longitudinal slip stiffness of the tire, C_s indicates the normalized longitudinal slip stiffness of the tire, α is the slip angle, s denotes the slip ratio, and κ and $f(\kappa)$ are determined by

$$\kappa = \frac{\mu F_z (1+|s|)}{2\sqrt{(C_k s)^2 + (C_\alpha \, tan\, \alpha)^2}} \tag{13}$$

$$f(\kappa) = \begin{cases} (2-\kappa)\kappa, & \kappa < 1 \\ 1, & \kappa \geq 1 \end{cases} \tag{14}$$

where μ denotes the nominal TRFC.

The major advantage of the Dugoff model is that the tire stiffness can be divided into longitudinal and lateral directions independently. However, different from the Magic Formula tire model, the precision of the Dugoff model drops significantly when the slip ratio is larger than 0.3 [28]. A modified Dugoff tire model is proposed to settle this issue. The pure longitudinal and lateral TRFCs are defined as shown below:

$$\mu_s = \mu_{xp} - (\mu_{xp} - \mu_{xs}) S_s \tag{15}$$

$$\mu_\alpha = \mu_{yp} - (\mu_{yp} - \mu_{ys}) S_\alpha \tag{16}$$

where μ_{xp} and μ_{yp} are the peak value of the longitudinal and lateral TRFCs, respectively. μ_{xs} and μ_{ys} represent the longitudinal and lateral sliding TRFCs, respectively. S_s and S_α are defined as

$$S_s = |s| \tag{17}$$

$$S_\alpha = \min\left(1, \ \frac{v_a sin|\alpha|}{max(v_a \, cos\alpha, \ u)}\right) \tag{18}$$

The slip ratio is redefined to ensure positive results even in braking conditions:

$$\lambda_{ij} = \begin{cases} \frac{\omega_{ij}R_{ij} - u}{\omega_{ij}R_{ij}} (u \leq \omega_{ij}R_i, \omega_{ij} \neq 0), & \text{acceleration} \\ \frac{u - \omega_{ij}R_{ij}}{u} (u > \omega_{ij}R_i, u \neq 0), & \text{braking} \end{cases} \tag{19}$$

2.3. Structure and DC Motor Model of the iEPB

The iEPB actuator consists of a DC motor, a belt drive, a gear reducer, a ball-screw assembly, a caliper, two friction pads, a piston, and an ECU to execute the lower-level algorithm. Two of the same iEPB actuators are installed separately in the left and right rear wheels, and an overall ECU is adopted to execute the upper-level algorithm to generate the desired clamping forces for both rear wheels. The DC motor affects the clamping force generation or regulation characteristics significantly, and the electrical equations of the DC motor are as follows:

$$\begin{cases} u_a V_a = E_b + R_a i_a + L_a \dot{i}_a \\ E_b = k_e \omega_{\mathrm{m}} \end{cases} \tag{20}$$

in which u_a denotes the pulse width modulation (PWM) duty, V_a is the motor nominal voltage, i_a represents the motor current, and ω_m is the motor rotational speed. E_b and k_e represent the counter electromotive voltage and constant, respectively. L_a and R_a indicate the phase-to-phase terminal inductance and resistance, accordingly. The system torque balance equations are described as follows:

$$\begin{cases} J_m \dot{\omega}_m = T_a - c_m \omega_m - T_m \\ T_a = k_t i_a \end{cases} \tag{21}$$

where J_m represents the motor rotational inertia, T_a is the motor electromagnetic torque, T_m denotes the load torque applied to the motor shaft, c_m stands for the motor damping coefficient, and k_t is the torque constant.

2.4. Screw-Nut and Caliper Mechanism Model

The screw rotates to move the nut forward or backward in the axial direction to regulate the clamping forces, and it can be described as

$$\theta_s = \frac{2\pi s_{nut}}{P_h} \tag{22}$$

where θ_s denotes the screw rotational angle, s_{nut} stands for the nut stroke, and P_h indicates the screw-nut pitch.

For precisely building the screw-nut model, the motion of the screw-nut assembly has been regarded as a slide block that moves along an inclined surface, as shown in Figure 1. d_1 and d_2 represent the inside and outside diameters of the screw, respectively, γ denotes the thread angle, F_N indicates the normal force, F_Q (clamping force) and F_H stand for the normal force distributed along the axial and radial directions, respectively, and v_s is the nut linear speed along with the inclined surface.

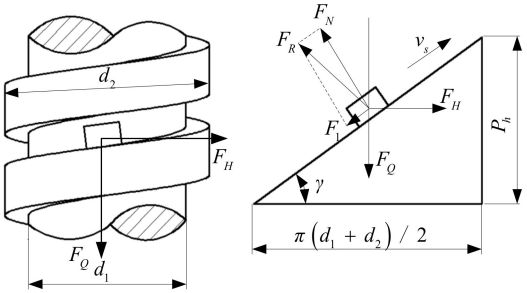

Figure 1. Schematic diagram between the screw and nut.

The force balance expressions are derived

$$\begin{cases} T_{screw} = F_H d/2 \\ F_{fs} = F_H cos\gamma - F_Q sin\gamma \\ F_{fc} = u_s\left(F_H sin\gamma + F_Q cos\gamma\right) \end{cases} \tag{23}$$

where T_{screw} stands for the screw driving torque, d denotes the medium diameter of the screw, F_{fs} is the friction force before the maximum static friction f_s has been overcome, F_{fc} represents the Coulomb friction force, and μ_s indicates the sliding friction coefficient.

The friction force generated by the contact surface inside the screw-nut assembly will affect the clamping force tracking performance significantly. Therefore, this paper concentrates on the static, Coulomb, viscous and Stribeck effects, and a simplified friction model is generated based on the Tustin model to improve control accuracy [29].

$$F_f = \begin{cases} F_{fs}, & v_s = 0 \text{ and } F_{fs} < f_s \\ \left(F_{fc} + \left(f_s - F_{fc}\right)e^{-|v_s|/v_{st}}\right)sgn(v) + f_v v_s, & \text{otherwise} \end{cases} \tag{24}$$

in which F_f denotes the total friction force, f_v is the viscous friction coefficient, and v_{st} stands for the Stribeck speed.

Figure 2 shows the Tustin friction curve and simplified fitting lines proposed in this paper. $\left(v_{ps}, F_f(v_{ps})\right)$ and $\left(v_{ns}, F_f(v_{ns})\right)$ are the intersection points of lines in positive and negative velocity regions, respectively. The slopes of the lines L_{p1}, L_{p2}, L_{n1}, L_{n2} are decided by $\left.\frac{\partial F_f}{\partial v_s}\right|_{v_s=0_+}$, $\left.\frac{\partial F_f}{\partial v_s}\right|_{v_s=v_{pmax}}$, $\left.\frac{\partial F_f}{\partial v_s}\right|_{v_s=0_-}$, and $\left.\frac{\partial F_f}{\partial v_s}\right|_{v_s=v_{nmax}}$, accordingly. v_{pmax} and v_{nmax} represent the maximum positive and negative velocities of the nut. Together with the points $\left(0_+, F_f(0_+)\right)$, $\left(v_{pmax}, F_f(v_{pmax})\right)$, $\left(0_-, F_f(0_-)\right)$ and $\left(v_{nmax}, F_f(v_{nmax})\right)$, the lines can be expressed as follows:

$$\begin{cases} F_{L_{p1}}(v_s) = \underbrace{\left(f_v - \dfrac{f_s - F_{fc}}{v_{st}}\right)}_{a_{p1}} v_s + \underbrace{f_{s+}}_{b_{p1}} \\ F_{L_{p2}}(v_s) = \underbrace{\left(f_v - \dfrac{f_s - F_{fc}}{v_{st}} e^{-v_{pmax}/v_{st}}\right)}_{a_{p2}} v_s + \underbrace{F_f(v_{pmax}) + \left(\dfrac{f_s - F_{fc}}{v_{st}} e^{-v_{pmax}/v_{st}} - f_v\right) v_{pmax}}_{b_{p2}} \\ F_{L_{n1}}(v_s) = \underbrace{\left(f_v + \dfrac{f_s - F_{fc}}{v_{st}}\right)}_{a_{n1}} v_s + \underbrace{f_{s-}}_{b_{n1}} \\ F_{L_{n2}}(v_s) = \underbrace{\left(f_v + \dfrac{F_s - F_{fc}}{v_{st}} e^{v_{nmax}/v_{st}}\right)}_{a_{n2}} v_s + \underbrace{F_f(v_{nmax}) - \left(\dfrac{f_s - F_{fc}}{v_{st}} e^{v_{nmax}/v_{st}} + f_v\right) v_{nmax}}_{b_{n2}} \end{cases} \tag{25}$$

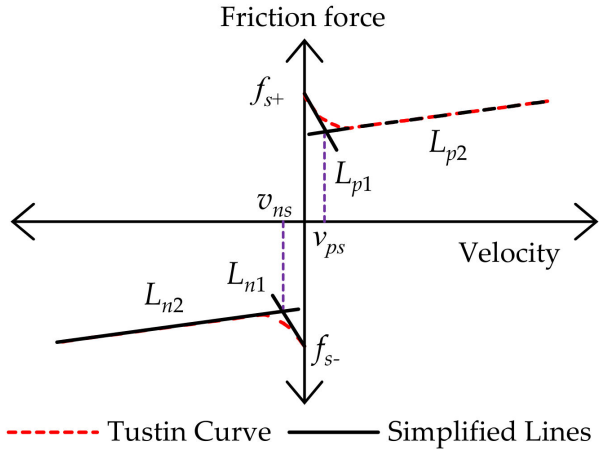

Figure 2. Tustin friction curve.

Equation (25) could be further simplified as

$$F_f(v_s) = \begin{cases} a_{p1}v_s + b_{p1}, & 0 \le v_s < v_{ps} \\ a_{p2}v_s + b_{p2}, & v_{ps} < v_s < v_{pmax} \\ a_{n1}v_s + b_{n1}, & v_{ns} \le v_s < 0 \\ a_{n2}v_s + b_{n2}, & v_{pmax} < v_s < v_{ns} \end{cases} \tag{26}$$

The parameters of the friction model had been identified through numerical experiments on an HIL test platform, and the nut moving speed was controlled to change from −50 to 50 mm/s with a resolution of 2 mm/s. Four lines were fitted through the experiment results employing the least square method, and the finally identified parameters are listed in Table 1.

Table 1. Identified parameters of the friction model.

Symbols	Value	Symbols	Value
a_{p1}	−3.12	b_{p1}	148.26
a_{p2}	2.35	b_{p2}	60.05
a_{n1}	−3.74	b_{n1}	−137.72
a_{n2}	2.97	b_{n2}	−55.79
v_{pm} (mm/s)	6.8	v_{nm} (mm/s)	−6.76
v_{pmax} (mm/s)	50	v_{nmax} (mm/s)	−50

2.5. Control-Oriented Transmission Mechanism Model

The mechanical diagram of the iEPB actuator is shown in Figure 3. Here, 1 and 2 indicate the driving and driven pulleys of the belt drive, respectively, while 3, 4 and 5 represent the sun gear, planet gear and planet carrier of the first planetary gear set, respectively. The numbers 6, 7 and 8 denote the sun gear, planet gear and planet carrier of the second planetary gear set, respectively, while 11 is the ring gear for both of the two planetary gear sets. The numbers 9 and 10 indicate the screw and nut of the ball-screw assembly. Lastly, 12, 13 and 14 are the pad, disc, and caliper, respectively. When parking or other active braking functions are requested, the gap between the pad and disc will be overcome firstly, and then the clamping force is generated.

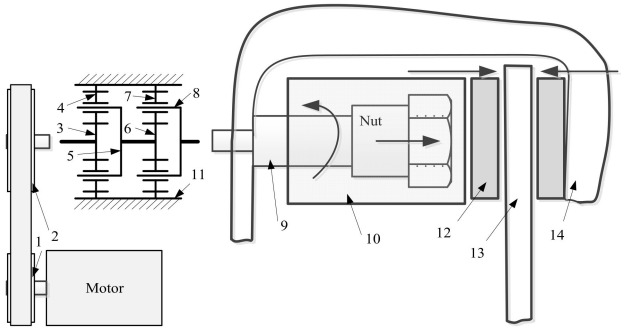

Figure 3. Mechanical diagram of the iEPB actuator.

When the braking function is applied, the dynamic motions of the iEPB system are described as follows:

$$\begin{cases} T_m = T_1 = J_{tm1}\dot{\omega}_{tm1} + c_{tm1}\omega_{tm1} + \frac{T_2}{\eta_{tm12}i_{tm12}} \\ T_2 = T_3 = J_{tm2}\dot{\omega}_{tm2} + J_{tm3}\dot{\omega}_{tm3} + c_{tm2}\omega_{tm2} + m_{tm4}r_{tm5}^2\dot{\omega}_{tm5} + NJ_{tm4}\dot{\omega}_{tm4} + \frac{T_5}{\eta_{tm35}i_{tm35}} \\ T_5 = T_6 = J_{tm5}\dot{\omega}_{tm5} + J_{tm6}\dot{\omega}_{tm6} + m_{tm7}r_{tm8}^2\dot{\omega}_{tm8} + Ni_{tm7}\dot{\omega}_{tm7} + \frac{T_8}{\eta_{tm68}i_{tm68}} \\ T_8 = J_{tm8}\dot{\omega}_{tm8} + c_{tm3}\omega_{tm8} + J_{tm9}\dot{\omega}_{tm9} + F_f(v_s)\frac{d}{2}\frac{1}{\eta_{tm98}} + \frac{F_Q P_h}{2\pi\eta_{tm98}} \end{cases} \tag{27}$$

When the braking function is released, the dynamic motions of the iEPB system can be expressed by the following equations

$$\begin{cases} T_m = T_1, T_1 - J_{tm1}\dot{\omega}_{tm1} - c_{tm1}\omega_{tm1} = \frac{\eta_{tm21}T_2}{i_{tm12}}, T_2 = T_3 \\ T_3 + J_{tm2}\dot{\omega}_{tm2} + J_{tm3}\dot{\omega}_{tm3} + c_{tm2}\omega_{tm2} + m_{tm4}r_{tm5}^2\dot{\omega}_{tm5} + NJ_{tm4}\dot{\omega}_{tm4} = \frac{\eta_{tm53}T_5}{i_{tm35}} \\ T_5 = T_6, T_6 + J_{tm5}\dot{\omega}_{tm5} + J_{tm6}\dot{\omega}_{tm6} + m_{tm7}r_{tm8}^2\dot{\omega}_{tm8} + NJ_{tm7}\dot{\omega}_{tm7} = \frac{\eta_{tm86}T_8}{i_{tm68}} \\ T_8 + J_{tm8}\dot{\omega}_{tm8} + c_{tm3}\omega_{tm8} + J_{tm9}\dot{\omega}_{tm9} + F_f(v_s)\frac{d}{2}\frac{1}{\eta_{tm89}} = \frac{F_Q P_h}{2\pi\eta_{tm89}} \end{cases} \tag{28}$$

where T, J_{tm}, ω_{tm}, m_{tm}, and r_{tm} stand for the torque, inertia, rotational speed, mass and radius of corresponding components, respectively, and the numerical subscripts stand for the corresponding components shown in Figure 3. η_{tm} and i_{tm} denote the transmission efficiency and ratio from the component corresponding to the first subscript to the component corresponding to the second subscript. N is the number of the planetary gears, while c_{tm1}, c_{tm2}, and c_{tm3} are the rotational damping coefficients of shaft-bearings of the driving pulley, driven pulley and second planet carrier, respectively.

The rotational speed equations are as follows:

$$\begin{cases} \frac{\omega_m}{i_{tm12}} = \frac{\omega_{tm1}}{i_{tm12}} = \omega_{tm2} = \omega_{tm3}, \omega_{tm4} = \left(1 + \frac{1}{i_{tm34}}\right)\omega_{tm5} - \frac{1}{i_{tm34}}\omega_{tm3} = \frac{\omega_{tm1}}{i_{tm14}}, \\ \omega_{tm6} = \omega_{tm5} = \frac{\omega_{tm3}}{i_{tm35}} = \frac{\omega_{tm1}}{i_{tm16}},\ \omega_{tm7} = \left(1 + \frac{1}{i_{tm68}}\right)\omega_{tm8} - \frac{1}{i_{tm68}}\omega_{tm6} = \frac{\omega_{tm1}}{i_{tm17}}, \\ \omega_{tm8} = \frac{\omega_{tm6}}{i_{tm68}} = \frac{\omega_{tm1}}{i_{tm18}}, i_{tm12} = \frac{Z_2}{Z_1},\ i_{tm35} = 1 + \frac{Z_{11}}{Z_3} = \frac{1}{i_{tm53}},\ i_{tm68} = 1 + \frac{Z_{11}}{Z_6} = \frac{1}{i_{tm86}} \end{cases} \tag{29}$$

where Z is the teeth number of corresponding components. According to Equations (27)–(29), the equivalent rotational damping coefficient c_{eq} and the equivalent inertia J_{eq} are determined by

$$c_{eq} = \begin{cases} c_{tm1} + \frac{c_{tm2}}{\eta_{tm12}i_{tm12}^2} + \frac{c_{tm3}}{\eta_{tm12}\eta_{tm35}\eta_{tm68}i_{tm12}i_{tm35}i_{tm68}i_{tm18}}, & \omega_m > 0 \\ c_{tm1} - \frac{\eta_{tm21}c_{tm2}}{i_{tm12}^2} - \frac{\eta_{tm21}\eta_{tm53}\eta_{tm86}c_{tm3}}{i_{tm12}i_{tm35}i_{tm68}i_{tm18}}, & \omega_m < 0 \end{cases} \tag{30}$$

$$J_{eq} = \begin{cases} J_{tm1} + \frac{1}{\eta_{tm12}}\left[H + \frac{1}{\eta_{tm35}}\left(K + \frac{1}{\eta_{tm68}}\frac{J_{tm8}+J_{tm9}}{i_{tm12}i_{tm35}i_{tm68}i_{tm18}}\right)\right], & \omega_m > 0 \\ J_{tm1} - \eta_{tm21}\left[H + \eta_{tm53}\left(K + \eta_{tm86}\frac{J_{tm8}+J_{tm9}}{i_{tm12}i_{tm35}i_{tm68}i_{tm18}}\right)\right], & \omega_m < 0 \end{cases} \tag{31}$$

where $H = \frac{J_{tm2}+J_{tm3}}{i_{tm12}^2} + \frac{Nm_{tm4}r_{tm5}^2}{i_{tm12}i_{tm15}} + \frac{NJ_{tm4}}{i_{tm12}i_{tm14}}$, $K = \frac{J_{tm5}+J_{tm6}}{i_{tm12}i_{tm35}i_{tm16}} + \frac{NJ_{tm7}}{i_{tm12}i_{tm35}i_{tm17}} + \frac{Nm_{tm7}r_{tm8}^2}{i_{tm12}i_{tm35}i_{tm18}}$.

Combining Equations (27)–(31), after some manipulations, we have

$$T_m = T_r + J_{eq}\dot{\omega}_m + c_{eq}\omega_m \tag{32}$$

$$T_r = \begin{cases} \frac{\pi d F_f(v_s) + F_Q P_h}{2\pi i_{tm12}i_{tm35}i_{tm68}\eta_{tm12}\eta_{tm35}\eta_{tm68}\eta_{tm89}}, & \omega_m \geq 0 \\ \frac{\eta_{tm21}\eta_{tm53}\eta_{tm86}\left(-\pi d F_f(v_s) + F_Q P_h\right)}{2\pi i_{tm12}i_{tm35}i_{tm68}\eta_{tm98}}, & \omega_m < 0 \end{cases} \tag{33}$$

in which T_r stands for the resistance torque at the motor shaft. Considering Equations (20), (21) and (32), we have

$$\begin{cases} \dot{\theta}_m = \omega_m \\ \dot{\omega}_m = -\frac{1}{J_t}T_r(\theta) - \frac{c_t}{J_t}\omega_m + \frac{k_t}{J_t}i_a \\ \dot{i}_a = -\frac{k_e}{L_a}\omega_m - \frac{R_a}{L_a}i_a + \frac{V_a}{L_a}u_a \end{cases} \tag{34}$$

where

$$\begin{cases} c_t = c_m + c_{eq} \\ J_t = J_m + J_{eq} \end{cases} \tag{35}$$

2.6. Brake Model

The braking torque can be defined in terms of the clamping force as

$$T_{epbr} = \mu_b r_p F_Q \tag{36}$$

where μ_b represents the friction coefficient between the pad and disc, and r_p denotes the equivalent radius from the pad to the disc center.

3. Sliding-Mode-Based Load Torque Observer

If the request braking deceleration exceeds the maximum force that the surface can provide, an ABS function should be triggered to maintain the vehicle stability and to shorten the braking distance. Therefore, we assume that the proposed strategy is used for realizing a semi-ABS function of the two rear wheels. A hierarchical control structure is designed, as shown in Figure 4. For realizing sensorless control of the lower level, an observer should be designed to estimate the load torque of the motor, and the estimation value will be adopted as the actual motor torque to achieve a closed-loop control of the motor.

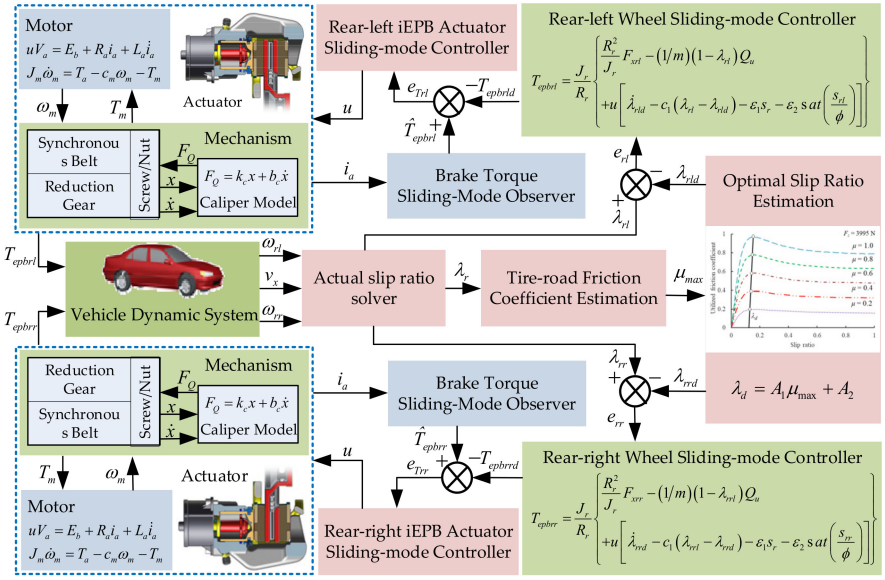

Figure 4. Hierarchical control structure.

The main sensitive parameters that affect the observer accuracy include the motor current i_a, the phase-to-phase terminal inductance L_a, the phase-to-phase terminal resistance R_a and the motor rotational speed ω_m. The execution cycle of the ECU, which is set to a frequency of 1 kHz in this paper, is very transient, and the load torque varies very slowly. Therefore, it is assumed that the load torque (or i_a) is non-variable within one control cycle [30]. L_a and R_a are reflected by Equation (20); ω_m is designed as the observation object. The dynamic equations of the DC motor, which is shown in Equations (33) and (34), can be converted into

$$\begin{cases} \dot{\omega}_m = \frac{k_t}{J_t} i_a - \frac{c_t}{J_t} \omega_m - \frac{1}{J_t} T_r \\ \dot{T}_r = 0 \end{cases} \tag{37}$$

The rotational speed and load torque-tracking errors are defined as follows:

$$\begin{cases} e_1 = \hat{\omega}_m - \omega_m \\ e_2 = \hat{T}_r - T_r \end{cases} \tag{38}$$

where $\hat{\omega}_m$ and $\hat{T}_r$ stand for the estimated rotational speed load torque, respectively. Shown in Equation (37) is a first-order control system, and the sliding surface is designed in terms of speed-tracking error

$$s = e_1 \tag{39}$$

Since the transfer function of Equation (39) is stable ($H(s) = 1$), if the sliding surface is controlled to remain small or converge to zero, then the tracking error e_1 will be adjusted to a small range. The SMO for rotational speed and load torque estimation is designed as

$$\begin{cases} \dot{\hat{\omega}}_m = \frac{k_t}{J_t} i_a - \frac{c_t}{J_t} \hat{\omega}_m - \frac{1}{J_t} \hat{T}_r + U \\ \dot{\hat{T}}_r = gU \end{cases} \tag{40}$$

where g is the feedback gain, and U is the control law. A piecewise linear approximation saturation function is adopted to eliminate the chattering problem as follows [31]:

$$U = Ksat(s/\Phi_1) \tag{41}$$

where $\Phi_1 \geq 0$ is the thickness of the boundary layer, $K > 0$ is the sliding-mode gain, and

$$sat(s/\Phi_1) = \begin{cases} s/\Phi_1, & |s/\Phi_1| < 1 \\ \mathrm{sgn}(s/\Phi_1), & |s/\Phi_1| \geq 1 \end{cases} \tag{42}$$

Substituting Equation (40) into Equation (38), after some manipulations, we have

$$\begin{cases} \dot{e}_1 = -\frac{c_t}{J_t}e_1 - \frac{1}{J_t}e_2 + U \\ \dot{e}_2 = gU \end{cases} \tag{43}$$

The following Lyapunov function is defined to discuss the stability of the SMO.

$$V = \frac{1}{2}s^2 \tag{44}$$

Thus,

$$\dot{V} = s\dot{s} \tag{45}$$

Considering Equations (39), (41) and (43), after some manipulations, we have

$$\dot{V} = -e_1 sat(e_1/\Phi_1)\left(\frac{c_t}{J_t}\frac{e_1}{sat(e_1/\Phi_1)} + \frac{1}{J_t}\frac{e_2}{sat(e_1/\Phi_1)} - K\right) \tag{46}$$

Apparently, $-e_1 sat(e_1/\Phi_1) \leq 0$, and the expression in the bracket should be nonnegative to ensure the stability of the controller. Thus, the sliding-mode gain is determined by

$$K \leq \frac{c_t}{J_t}\frac{e_1}{sat(e_1/\Phi_1)} + \frac{1}{J_t}\frac{e_2}{sat(e_1/\Phi_1)} \tag{47}$$

If we assume that the tracking errors e_1 and e_2 are separately positive and negative, Equation (47) could be further expressed as

$$K \leq \begin{cases} (\Phi_1/J_t)(c_t - |e_2/e_1|), & |e_1/\Phi_1| < 1 \\ (c_t/J_t)|e_1| - (1/J_t)|e_2|, & |e_1/\Phi_1| \geq 1 \end{cases} \tag{48}$$

According to Equation (46), s will arrive at the sliding surface $s = 0$ within a limited time if we assume that the beginning error $e_1(0)$ is finite, and therefore the speed-tracking error e_1 will converge to 0 when the proposed SMO falls into the surface. When $e_1 = 0$, Equation (43) could be further simplified as

$$\dot{e}_2 - \frac{g}{J_t}e_2 = 0 \tag{49}$$

Thus, the load torque observation error is determined by

$$e_2 = Ce^{\frac{g}{J_t}t} \tag{50}$$

in which C is a constant, and t is the total observation time. g/J_t should be negative for adjusting e_2 to converge to zero. To this effect, g will determine the attenuation rate of e_2, and it has to be negative.

4. Hierarchical Semi-ABS Controller Design

As shown in Figure 4, the upper controller is designed to track the DSR to fully utilize the road condition, and the desired braking torques for rear wheels are derived using the SMC technique; at the lower level, the motor is controlled to implement the desired braking torque that resulted from the upper controller. The desired clamping forces are finally

obtained by Equation (36) and the braking torques, and the actual clamping forces are calculated based on the load torque estimation results and the iEPB mechanism model.

4.1. Upper Controller

The slip ratios of the rear wheels are calculated with rear wheel rotational speeds and vehicle speed, which is observed by the electronic stability control algorithm (integrated into the iEPB's ECU). A TRFC observer is designed according to the μ-slip curve and experimental calibration parameters, and furthermore, the DSR is estimated from the characteristics of the utilized friction coefficient and the slip ratio. The upper controller is proposed to generate the desired braking torques to maintain the rear slip ratio tracking errors within a small range or converged to zero.

For both two rear wheels, the slip ratio-tracking error e_r is determined by the actual one λ_r and the desired one λ_{rd} as

$$e_r = \lambda_r - \lambda_{rd} \tag{51}$$

The sliding surface s_r is designed as

$$s_r = e_r + C_1 \int_0^t e_r(\tau) d\tau \tag{52}$$

where C_1 is a positive coefficient. Since the transfer function $H(s) = \frac{e_r(s)}{s_r(s)} = \frac{C_1 s}{C_1 s+1}$ is stable, the tracking error e_r will converge to 0 if the sliding surface is controlled to converge to 0.

The first derivative of s_r is derived as follows:

$$\dot{s}_r = \dot{e}_r + C_1 e_r = \dot{\lambda}_r - \dot{\lambda}_{rd} + C_1 e_r \tag{53}$$

The reaching law has been defined in terms of a piecewise linear approximation saturation function as

$$\dot{s}_r = -\varepsilon_1 s_r - \varepsilon_2 sat\left(\frac{s_r}{\Phi_2}\right) \tag{54}$$

where ε_1, ε_2 are positive sliding-mode gain factors, and $\Phi_2 \geq 0$ is the thickness of the boundary layer. $sat(s_r/\Phi_2)$ has the same definition as shown in Equation (42).

It is assumed that the hydraulic braking is not activated, which means that T_{br} is equal to 0. With Equations (5), (10) and (19), after some manipulations, we have

$$\begin{aligned} \dot{\lambda}_r &= \frac{\omega_r R_r \dot{u}}{u^2} - \frac{\dot{\omega}_r R_r}{u} = \frac{(1-\lambda_r)\dot{u}}{u} - \frac{R_r}{u}\dot{\omega}_r \\ &= (1/mu)(1-\lambda_r)Q_u - (R_r/J_r u)\Big(R_r F_{xr} - T_{epbr}\Big) \end{aligned} \tag{55}$$

Substituting Equation (55) into Equation (53), yields

$$\dot{s}_r = (1/mu)(1-\lambda_r)Q_u - (R_r/J_r u)\Big(R_r F_{xr} - T_{epbr}\Big) - \Big[\dot{\lambda}_{rd} - c_1(\lambda_r - \lambda_{rd})\Big] \tag{56}$$

The control law is defined as

$$T_{epbr} = \frac{J_r}{R_r}\left\{\frac{R_r^2}{J_r}F_{xr} - (1/m)(1-\lambda_r)Q_u + u\left[\dot{\lambda}_{rd} - c_1(\lambda_r - \lambda_{rd}) - \varepsilon_1 s_r - \varepsilon_2 sat\left(\frac{s_r}{\Phi_2}\right)\right]\right\} \tag{57}$$

The Lyapunov function is designed as

$$V = \frac{1}{2}s_r^2 \tag{58}$$

Thus,

$$\begin{aligned} \dot{V} &= s_r \dot{s}_r = s_r\Big\{-(R_r/J_r u)\Big(R_r F_{xr} - T_{epbr}\Big) + (1/mu)(1-\lambda_r)Q_u - \Big[\dot{\lambda}_{rd} - c_1(\lambda_r - \lambda_{rd})\Big]\Big\} \\ &= -s_r\Big(\varepsilon_1 s_r + \varepsilon_2 sat\Big(\tfrac{s_r}{\Phi_2}\Big)\Big) = -\varepsilon_1 s_r^2 - \varepsilon_2 |s_r| < 0 \end{aligned} \tag{59}$$

According to the assumptions and Equation (59), the upper controller is stable and s_r will arrive the sliding surface within a limited time if we assume that the beginning error $e_r(0)$ is finite, and then a continuous function is adopted to eliminate the chattering problem when inside the boundary layer $|s_r/\Phi_2| < 1$. It is assumed that Equation (59) holds until $|s_r| > \Phi_{2\min}$, and $\Phi_{2\min}$, which is determined by the system disturbances, is the thickness of the thinnest boundary layer. The price for eliminating chattering and achieving a smooth control law is a loss of precision, and the ensured accuracy is decided by $|e_r(t)| \leq (\Phi_{2\min} - C_1 C_{ct})/(C_1 t + 1)$, where C_{ct} is the constant of integration, and t is the total convergence time.

4.2. Lower Controller

The main sensitive parameters that affect the lower control performance include the motor load torque, the mechanical transmission, the mechanical friction and the disturbances. The load torque is estimated by the proposed observer, and the detail control-oriented mechanical transmission model is established in Section 2.5. The mechanical friction characteristics is simplified into four fitting lines to create an online friction estimation model, as illustrated in Section 2.4. An SMC-based braking torque controller, which is insensitive to disturbances and uncertainties, is proposed in lower level, by which the actual braking torque will be adjusted to follow the desired one generated from the upper level; the actual braking torque is calculated by the designed SMO. The motor terminal inductance L_a is very small, and it is assumed to be negligible; the braking torque can be described with Equations (20), (33), (34) and (36)

$$\begin{cases} \omega_m \geq 0 : T_{epbr} = H_1 H_2 \left(M_1 u_a - M_2 \omega_m - J_t \dot{\omega}_m\right) - H_1 \pi d F_f(v_s) \\ \omega_m < 0 : T_{epbr} = H_1 H_3 \eta_n \left(M_1 u_a - M_2 \omega_m - J_t \dot{\omega}_m\right) + H_1 \pi d F_f(v_s) \end{cases} \tag{60}$$

and

$$\begin{cases} H_1 = \frac{\mu_b r_p}{P_h}, \eta_n = \frac{1}{\eta_{21}\eta_{53}\eta_{86}}, \ M_1 = \frac{k_t V_a}{R_a}, M_2 = \frac{k_t k_e + c_n R_a}{R_a} \\ H_2 = 2\pi i_{tm12} i_{tm35} i_{tm68} \eta_{tm35} \eta_{tm68} \eta_{tm89}, H_3 = 2\pi i_{tm12} i_{tm35} i_{tm68} \eta_{tm98} \end{cases} \tag{61}$$

We define the braking torque-tracking error as follows:

$$e_T = \hat{T}_{epbr} - T_{epbrd} \tag{62}$$

where T_{epbrd} stands for the desired braking torque, and the sliding surface S_T is defined as

$$s_T = C_2 e_T + \int_0^t e_T(\tau) dt \tag{63}$$

where C_2 is a positive constant; deriving Equation (63) WRT time, we have

$$\dot{s}_T = C_2 \dot{e}_T + e_T = C_2 \dot{e}_T + \hat{T}_{epbr} - T_{epbrd} \tag{64}$$

The reaching law is designed as follows:

$$\dot{s}_T = -\varepsilon_3 s_T - \varepsilon_4 sat\left(\frac{s_T}{\Phi_3}\right) \tag{65}$$

where ε_3 and ε_4 are positive sliding-mode gain factors, and $\Phi_3 \geq 0$ is the thickness of the boundary layer. Substituting Equation (60) into Equation (64), after some manipulations, yields

$$\begin{cases} \omega_m \geq 0 : \dot{s}_T = C_2 \left(\dot{\hat{T}}_{epbr} - \dot{T}_{epbrd}\right) - T_{epbrd} + H_1 H_2 \left(M_1 u_a - M_2 \omega_m - J_t \dot{\omega}_m\right) - H_1 \pi d F_f(v_s) \\ \omega_m < 0 : \dot{s}_T = C_2 \left(\dot{\hat{T}}_{epbr} - \dot{T}_{epbrd}\right) - T_{epbrd} + H_1 H_3 \eta_n \left(M_1 u_a - M_2 \omega_m - J_t \dot{\omega}_m\right) + H_1 \pi d F_f(v_s) \end{cases} \tag{66}$$

The control law is defined as

$$\begin{cases} \omega_m \geq 0 : u_a = \left\{ \begin{array}{l} H_1H_2\left(M_2\omega_m + J_t\dot{\omega}_m\right) + H_1\pi dF_f(v_s) + T_{epbrd} \\ -C_2\left(\dot{\hat{T}}_{epbr} - \dot{T}_{epbrd}\right) - \varepsilon_3 s_T - \varepsilon_4 sat\left(\frac{s_T}{\Phi_3}\right) \end{array} \right\} / H_1H_2M_1 \\ \omega_m < 0 : u_a = \left\{ \begin{array}{l} H_1H_2\eta_n\left(M_2\omega_m + J_t\dot{\omega}_m\right) - H_1\pi dF_f(v_s) + \\ T_{epbrd} - C_2\left(\dot{\hat{T}}_{epbr} - \dot{T}_{epbrd}\right) - \varepsilon_3 s_T - \varepsilon_4 sat\left(\frac{s_T}{\Phi_3}\right) \end{array} \right\} / H_1H_2M_1\eta_n \end{cases} \tag{67}$$

The Lyapunov function is designed as

$$V = \frac{1}{2}s_T^2 \tag{68}$$

Deriving Equation (68), considering Equation (65), we have

$$\dot{V} = s_T\dot{s}_T = -s_T(\varepsilon_3 s_T + \varepsilon_4 sat(s_T/\Phi_3)) = -\varepsilon_3 s_T^2 - \varepsilon_4|s_T| < 0 \tag{69}$$

5. Experimental Test and Analysis

The proposed algorithm is evaluated in this section through realizing semi-ABS functions. To this end, firstly, a real-time HIL test bench installed with iEPB prototypes was developed. Subsequently, a lot of vehicle dynamic experiments, including single-lane-change, double-lane-change, steady-state cornering, step response, pylon course slalom, transition brake and split brake maneuvers, were conducted to calibrate the vehicle model, and the final adjusted parameters were derived to enhance the model accuracy using the experimental results. Ultimately, semi-ABS experiments were conducted on the real-time HIL test bench to evaluate the effectiveness and accuracy of the presented controller.

5.1. HIL Test Bench Design

Figure 5 shows the HIL test bench. The industrial personal computer (IPC) runs TASS International PreSCAN 8.5.0 to provide experimental animation and environmental sensing data. The operation monitor displays the experimental data and the maneuver configuration options, and the scenario monitor is used to display the experimental animation. The dSPACE SCALEXIO is employed to run the vehicle model in real time and to sample signals from underlying actuators. The T-Booster actuator, which generates hydraulic braking pressure with an electric motor and a transmission mechanism, is adopted to amplify the driver's brake effort or to realize active braking functions in special conditions. The EPS actuator can amplify the driver's steering effort and implement active steering control. The proposed algorithm code is generated from the MATLAB/Simulink block diagrams, and the generated code is downloaded to the ECU that includes a low-cost MCU, NXP SPC5744, several communication and power amplifier chips. The MCU executes the proposed algorithm for iEPB prototype control and samples signals at a rate of 1 kHz.



Figure 5. HIL test bench.

5.2. Vehicle Model Validation and Modification

The JAC iEV7S model, which is a four-wheel double-drive electric passenger car produced by a Chinese automotive manufacturing company named Anhui Jianghuai Automobile Co., Ltd., was firstly employed for vehicle model calibration. Furthermore, experimental devices were installed inside or outside the dynamic test vehicle as shown in Figure 6, and various dynamic experiments under different maneuvers were carried out. Ultimately, the vehicle model was modified with the test results, and a set of finely tuned parameters of the vehicle model were determined, as shown in Table 2.



Figure 6. Experimental vehicle and devices.

Table 2. Vehicle parameters.

Parameters	Value
Vehicle mass (m)	1855 kg
Tire radius (R_f, R_r)	316 mm
Rotational inertia of the front/rear tire (J_f, J_r)	1.5 kg•m^2
Height of the center of gravity (h_g)	530 mm
Distance between the front and rear axles (t_w)	2490 mm
Front axle to the center of gravity (a)	1100 mm
Rear axle to the center of gravity (b)	1390 mm
Brake disc friction coefficient (u_b)	0.35
Effective brake disc radius (r_p)	105 mm

The lateral acceleration and yaw rate, which are the two most essential factors to reveal body stability during manipulating the vehicle, are selected to give a comprehensive judgement between the experimental and simulation results. Figure 7 shows the test and simulation results under the pylon course slalom maneuver. The root-mean-square (RMS) error of lateral acceleration between the experiment and simulation is 0.08 m/s^2, whereas that of the yaw rate is 0.01 rad; the vehicle model's accuracy reflected by lateral acceleration and yaw rate is 98% and 95%, respectively. Thus, the modified vehicle model can precisely reflect the vehicle dynamics and it is reasonable for it to be employed in the real-time HIL experiments.

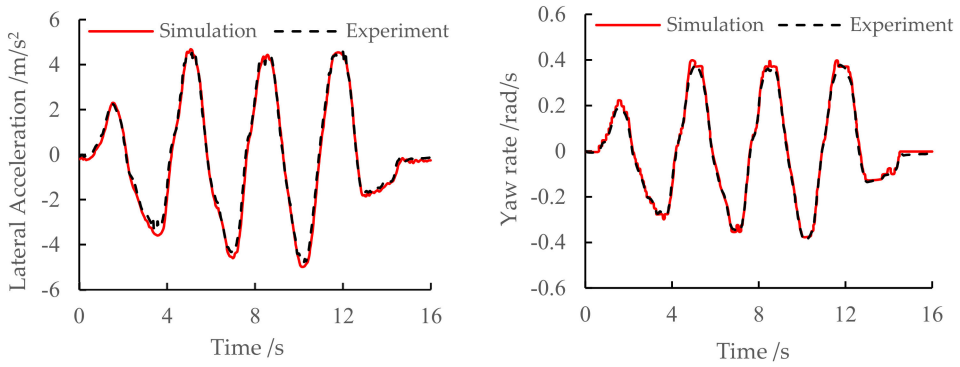

Figure 7. Experimental and simulation results achieved under pylon course slalom maneuver: (**a**) lateral acceleration; (**b**) yaw rate.

5.3. Experimental Validation of the Load Torque Observer

Experiments were conducted to validate whether the designed observer is effective. The motor target rotational speed is 300 rad/s, and the motor is abruptly loaded and unloaded at run time. As shown in Figure 8, the estimated load torque matches very well with the actual one, although the usage of low accuracy encoder leads to a large rotational speed measurement error. This indicates that the proposed observer is effective and robust in dealing with signal fluctuations.

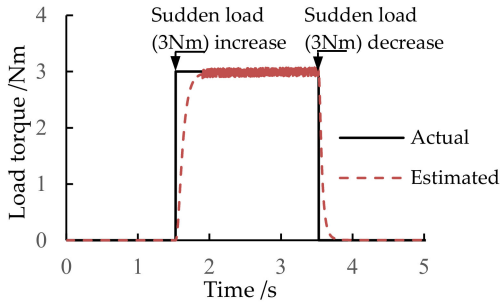

Figure 8. The comparison between the actual and estimated load torque.

5.4. Experiment Results and Analysis of the Proposed Controller

Numerical experiments were carried out on the HIL test bench to evaluate the proposed algorithm under homogenous surface, transition surface and split surface maneuvers.

5.4.1. Straight-line Braking on High-μ Homogeneous Surface

Figure 9 indicates the results achieved under the straight-line braking on a homogeneous surface maneuver at a longitudinal velocity of 100 km/h and with a high TRFC of 0.8. Figure 9(1) shows the actual and estimated TRFCs; the estimated TRFC can track the actual one well and quick, and the steady-state error (SSE) is under 0.03. However, the TRFC observer is designed according to the μ-slip experience curve, and the curve is divided into three regions to derive corresponding simplified expressions using different slope ranges, and the slope ranges, which are calibrated by road experiments, may vary slightly on different road surfaces. These tiny parameter errors will lead to a decrease in the accuracy of the observer, especially on a high-μ surface. As shown in Figure 9(1), the estimation error is increased after about 19 s. Nevertheless, the estimation error is within a reasonable range for the proposed controller.

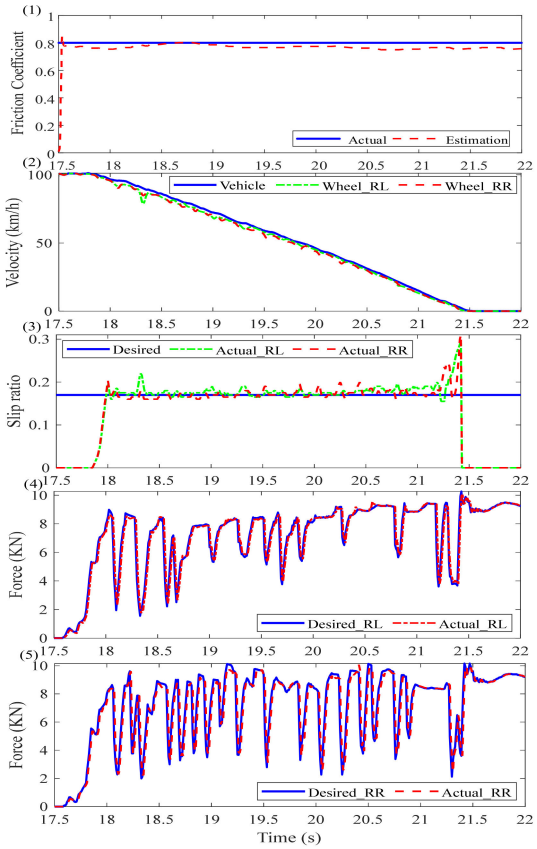

Figure 9. HIL test results achieved under a high adhesion coefficient maneuver (vehicle longitudinal speed = 100 km/h, μ = 0.8): (**1**) TRFC estimation; (**2**) velocities of vehicle and wheels; (**3**) slip ratios; (**4**) clamping forces of RL; (**5**) clamping forces of RR.

The time histories of the vehicle and wheel velocities derived from the model are shown in Figure 9(2); the vehicle is well controlled with the intervention of the proposed upper controller to avoid the rear wheels from locking up. Figure 9(3) illustrates the actual slip ratios of the rear wheels to following the desired one. The controlled actual slip ratios fluctuate frequently but slightly during the whole braking maneuver to help the rear wheels remain anti-locked successfully.

Figure 9(4),(5) reveal the clamping force tracking performance of the lower controller. The desired clamping forces of the rear wheels are calculated with Equation (36) using the desired braking torque generating from the upper controller, and the actual clamping forces are estimated by the proposed SMO and the iEPB mechanism model. The actual clamping forces track the desired ones quite well without obviously fluctuation throughout the whole braking maneuver, and the RMS force tracking errors of RL and RR wheels are separately 0.19 kN and 0.35 kN.

5.4.2. Straight-Line Braking on Low-μ Homogeneous Surface

To examine the algorithm performance under different TRFCs, Figure 10 shows the results derived under straight-line braking on a homogeneous surface maneuver at a longitudinal speed of 100 km/h and with a low TRFC of 0.2. Figure 10(1) illustrates the time histories of the actual and estimated TRFCs; it achieves a better estimation performance than high TRFC maneuvers. The RMS force tracking errors of RL and RR wheels are 0.13 kN and 0.14 kN, respectively.

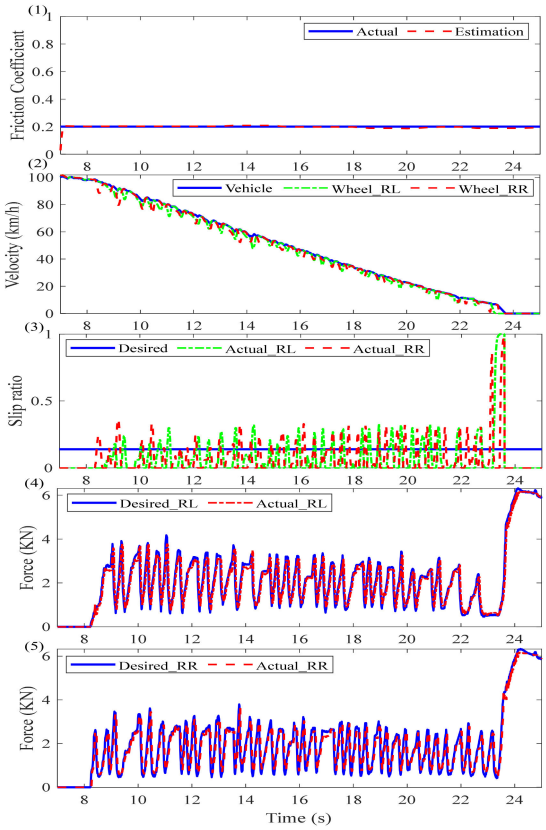

Figure 10. HIL test results achieved under a low adhesion coefficient maneuver (vehicle longitudinal speed = 100 km/h, μ = 0.2): (**1**) TRFC estimation; (**2**) velocities of vehicle and wheels; (**3**) slip ratios; (**4**) clamping forces of RL; (**5**) clamping forces of RR.

In most of the braking process, the clamping forces of the RL and RR wheels regulate more frequently on a low TRFC road than that on a high one. Figure 10 reveals that the clamping force increasement times of the RL and RR wheels are 31 and 38 in approximately 6 s, whereas that of Figure 9 are 14 and 19 in about 4 s. As indicated in Figure 10(3), the slip ratios of RL and RR wheels change quickly due to regulation of clamping forces, which could be clearly seen when the clamping forces are decreased at about 9.8 s and 21.8 s. Although the slip ratio changes dramatically owing to the clamping force regulation, it is within a reasonable range, which always keeps the wheels in anti-lock status, as illustrated in Figure 10(2).

5.4.3. Straight-Line Braking on μ-Jump Surface

Straight-line braking under a low-to-high μ surface was conducted to examine the proposed algorithm under a road friction coefficient step variation maneuver. Figure 11(1) indicates the time histories of the actual TRFC and the estimated one, a small estimation overshoot occurs at the road friction coefficient step change point due to rapid tracking performance, and the SSE of estimation is less than 0.04. The vehicle and wheel velocities generated on this maneuver are presented in Figure 11(2); the vehicle velocity reduces slowly, while the wheel velocities drop faster on a low adhesion coefficient surface before 9.4 s, and then the vehicle velocity decreases fast. As a result, the road adhesion coefficient suddenly increases to 0.8 after 9.4 s. Since the wheels are more likely to lock up on a low-adhesion road, Figure 11(3) shows that the slip ratios derived from the low-adhesion coefficient road regulate more sharply than those generated from the high-adhesion coefficient road. Figure 11(4),(5) shows the time histories of the RL and RR clamping forces, which exhibit the clamping force tracking performance in response to adhesion coefficient step variation. The desired clamping forces have been increased on the high TRFC road after about 9.4 s, and the RMSE of the RL and RR wheels are 0.09 kN and 0.1 kN, which re-

veals that the proposed controller achieves sufficient clamping force tracking performance.

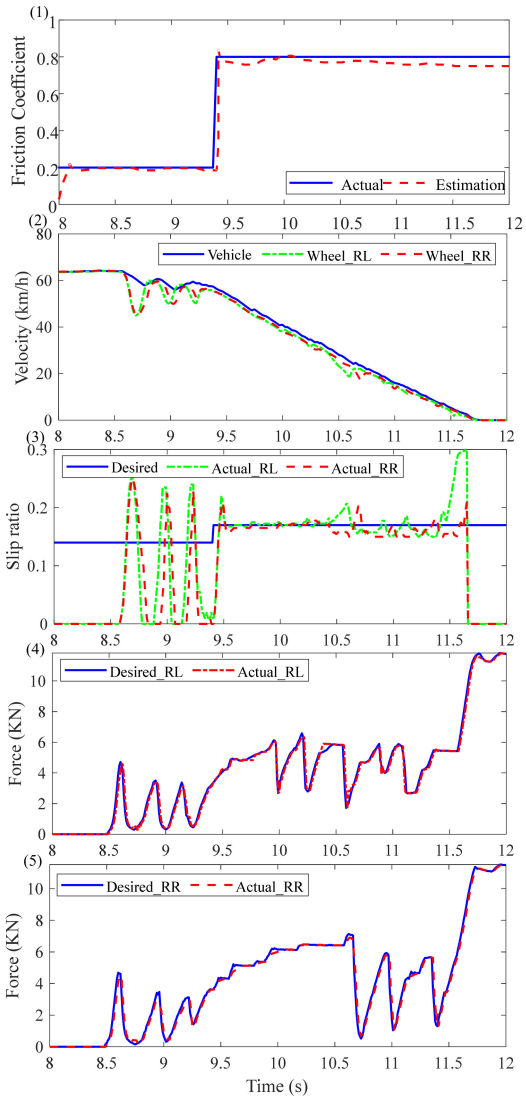

Figure 11. HIL test results achieved under a low-to-high μ surface maneuver (vehicle longitudinal speed = 60 km/h, μ = 0.2 to 0.8): (**1**) TRFC estimation; (**2**) velocities of vehicle and wheels; (**3**) slip ratios; (**4**) clamping forces of RL; (**5**) clamping forces of RR.

5.4.4. Straight-Line Braking on μ-Split Surface

Figure 12 shows the results derived from the straight-line braking on a μ-split surface maneuver at a vehicle longitudinal velocity of 50 km/h with a left-side low-μ of 0.2 and right-side high-μ of 0.8. The estimation performance in coping with TRFC variation is shown in Figure 12(1); it is indicated that the estimated TRFCs of both the left and right sides match with the actual ones very well without remarkable tracking errors throughout the whole test maneuver. A close observation of velocities and slip ratios shown in Figure 12(2),(3) reveals that the RL wheel more easily lock up on a low-μ road due to slip ratio's dramatic fluctuations, whereas the RR wheel is not inclined to lock up on a high-μ road with a desirable slip ratio.

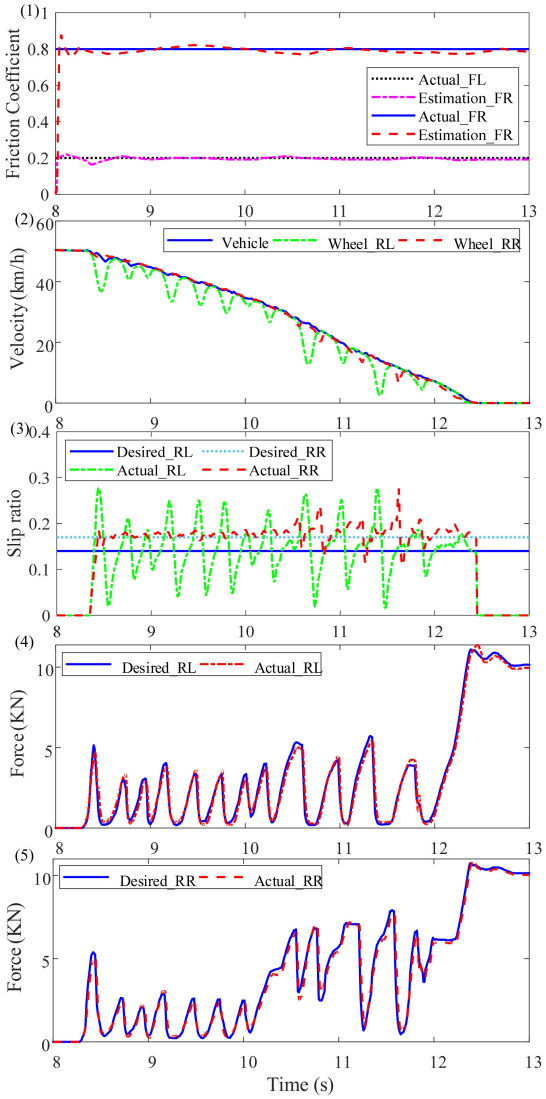

Figure 12. HIL test results achieved under a μ-split surface maneuver (vehicle longitudinal speed = 50 km/h, left-side μ = 0.2, right-side μ = 0.8): (**1**) TRFC estimation; (**2**) velocities of vehicle and wheels; (**3**) slip ratios; (**4**) clamping forces of RL; (**5**) clamping forces of RR.

As shown in Figure 12(4),(5), the RMS clamping force tracking errors of the RL and RR wheels are 0.11 kN and 0.13 kN, respectively, which ensures sufficient tracking performance. The peak tracking error (PTE) occurs, at which the clamping force changes to decrease or increase, for example at the certain moments of t = 9.6 s, t = 10 s, etc. in Figure 12(4), and at the certain moments of t = 8.4 s, t = 10.8 s, etc. in Figure 12(5). Once the direction of the clamping force increase changes, which means the iEPB motor changes direction, it will give rise to a direction turning of the friction. Conversely, the direction change in friction may lead to generate PTEs.

6. Conclusions

A hierarchical control strategy was developed to address the semi-ABS control problem of the rear wheels as well as the precise clamping force control issue without a clamping force sensor. An HIL system integrated with iEPB actuators and an algorithm was established to implement real-time experiments to verify and evaluate the proposed strategy, putting particular focus on vehicle model validation and modification to enhance the model's accuracy and thereby ensuring the reliability and validity of the HIL experiment results. The experimental results imply that the proposed SMO is effective for load torque estimation and reasonably robust in coping with signal fluctuation, the estimation error is

less than 2%, and the TRFC observer can constrain the error within 5%. The semi-ABS function experimental results show that the upper controller can rapidly generate the desired clamping forces for left and right rear wheels under different road surface conditions, and the lower controller provides a satisfactory performance in terms of tracking the designed clamping forces while maintaining the fluctuation in a small range. The proposed method provides the potential for an iEPB system to implement a secondary braking function if the primary braking system fails, or to realize active braking, or even to develop an anti-lock braking control system in practice.

Nonlinear characteristics and uncertainties always existed in iEPB control systems, such as estimation errors, measurement noise and mechanical friction. The SMC-based controller has low sensitivity to plant parameter variations and uncertainties, which decreases the requirement of model accuracy. Therefore, robust SMC-based controllers are designed in this paper. However, to eliminate the chattering problem, the thinnest boundary layer, which is determined by the uncertainties, is generated by employing a continuous reaching law, and the price for eliminating chattering and achieving a smooth control law is a loss of control precision. Thus, our future work will concentrate on the further improvement of control accuracy with the consideration of uncertainties. Moreover, the iEPB system could only realize a semi-ABS function since only the two rear wheels are equipped with iEPB systems in production vehicles. Hence, our future work will also focus on the cooperative control of the proposed iEPB system and regenerative braking system or electro-hydraulic braking system [32] to implement four-wheel-ABS function.

Author Contributions: Conceptualization, J.Y. and L.L.; methodology, J.Y. and D.W.; software, J.Y. and D.W.; validation, J.Y., L.L. and D.W.; formal analysis, Y.L.; investigation, J.Y.; resources, Y.L.; data curation, J.Y and D.W.; writing—original draft preparation, J.Y.; writing—review and editing, J.Y. and L.L.; visualization, Y.L.; supervision, L.L. and Y.L.; project administration, D.W.; funding acquisition, J.Y. All authors have read and agreed to the published version of the manuscript.

Funding: This research was funded by the National Natural Science Foundation of China (No. 52002009), Beijing Natural Science Foundation (No. 3222003), and the State Key Laboratory of Automotive Safety and Energy under Project No. KF2010.

Data Availability Statement: The data that support the findings of this study are available from the corresponding author upon reasonable request.

Conflicts of Interest: Author Mr. Dongliang Wang was employed by the company Trinova-Tech Co., Ltd., Tianjin. The remaining authors declare that the research was conducted in the absence of any commercial or financial relationships that could be construed as a potential conflict of interest.

References

1. Wang, B.; Guo, X.X.; Zhang, W.; Chen, Z.F. A study of an electric parking brake system for emergency braking. *Int. J. Veh. Des.* **2015**, *67*, 315–346. [CrossRef]
2. Zhang, L.; Yu, W.; Zhao, X.; Meng, A.H.; Fahad, M. Force-tracking control of a novel electric parking brake actuator based on a load-sensing, continuously variable transmission. *Proc. Inst. Mech. Eng. Part D J. Automob. Eng.* **2016**, *230*, 1569–1582. [CrossRef]
3. He, Z.J.; Shi, Q.; Wei, Y.J.; Gao, B.Z.; Zhu, B.; He, L. A model predictive control approach with slip ratio estimation for electric motor anti-lock braking of battery electric vehicle. *IEEE Trans. Ind. Electron.* **2022**, *69*, 9225–9234. [CrossRef]
4. Jung, S.; Kim, T.; Yoo, W. Advanced slip ratio for ensuring numerical stability of low-speed driving simulation Part I: Longitudinal slip ratio. *Proc. Inst. Mech. Eng. Part D J. Automob. Eng.* **2019**, *233*, 2903–2911. [CrossRef]
5. Jia, F.J.; Liu, Z.Y.; Zhou, H.J.; Chen, W. A novel design of traction control based on a piecewise-linear parameter-varying technique for electric vehicles with in-wheel motors. *IEEE Trans. Veh. Technol.* **2018**, *67*, 9324–9336. [CrossRef]
6. Li, W.F.; Du, H.P.; Li, W.H. Four-wheel electric braking system configuration with new braking torque distribution strategy for improving energy recovery efficiency. *IEEE Trans. Intell. Transp. Syst.* **2020**, *21*, 87–103. [CrossRef]
7. Milad, J.; Ehsan, H.; Amir, K.; Shih-ken, C.; Bakhtiar, L. A combined-slip predictive control of vehicle stability with experimental verification. *Veh. Syst. Dyn.* **2018**, *56*, 319–340.
8. Li, Z.H.; Wang, P.; Liu, H.H.; Hu, Y.F.; Chen, H. Coordinated longitudinal and lateral vehicle stability control based on the combined-slip tire model in the MPC framework. *Mech. Syst. Signal Process* **2021**, *161*, 107947. [CrossRef]
9. Liu, Y.H.; Li, T.; Yang, Y.Y.; Wu, J. Estimation of tire-road friction coefficient based on combined APF-IEKF and iteration algorithm. *Mech. Syst. Signal Process* **2017**, *88*, 25–35. [CrossRef]

10. Hu, J.Q.; Subhash, R.; Zhang, Y.M. Real-time estimation of tire-road friction coefficient based on lateral vehicle dynamics. *Proc. Inst. Mech. Eng. Part D J. Automob. Eng.* **2020**, *234*, 2444–2457. [CrossRef]
11. Feng, Y.C.; Chen, H.; Zhao, H.Y.; Zhou, H. Road tire friction coefficient estimation for four wheel drive electric vehicle based on moving optimal estimation strategy. *Mech. Syst. Signal Process* **2020**, *139*, 106416. [CrossRef]
12. Ramdane, T.; Driss, B.; Zheng, G.; Frédéric, K.; Rachid, E.G. Rotor speed, load torque and parameters estimations of a permanent magnet synchronous motor using extended observer forms. *IET Control Theory Appl.* **2017**, *11*, 1485–1492.
13. Kchaou, M.; Jerbi, H. Reliable H_∞ and passive fuzzy observer-based sliding mode control for nonlinear descriptor systems subject to actuator failure. *Int. J. Fuzzy Syst.* **2022**, *24*, 105–120. [CrossRef]
14. Kchaou, M.; Regaieg, M.A.; Al-Haijaji, A. Quantized asynchronous extended dissipative observer-based sliding mode control for Markovian jump TS fuzzy systems. *J. Franklin Inst.* **2022**, *359*, 9636–9665. [CrossRef]
15. Kchaou, M.; Jerbi, H.; Abassi, R.; VijiPriya, J.; Hmidi, F.; Kouzou, A. Passivity-based asynchronous fault-tolerant control for nonlinear discrete-time singular Markovian jump systems: A sliding-mode approach. *Eur. J. Control* **2021**, *60*, 95–113. [CrossRef]
16. Lian, C.Q.; Xiao, F.; Gao, S.; Liu, J.L. Load torque and moment of inertia identification for permanent magnet synchronous motor drives based on sliding mode observer. *IEEE Trans. Power Electron.* **2019**, *34*, 5675–5683. [CrossRef]
17. Zhang, X.G.; Cheng, Y.; Zhao, Z.H.; He, Y.K. Robust model predictive direct speed control for SPMSM drives based on full parameter disturbances and load observer. *IEEE Trans. Power Electron.* **2020**, *35*, 8361–8373. [CrossRef]
18. Lu, W.Q.; Zhang, Z.Y.; Wang, D.; Lu, K.Y.; Wu, D.; Ji, K.H.; Guo, L. A new load torque identification sliding mode observer for permanent magnet synchronous machine drive system. *IEEE Trans. Power Electron.* **2019**, *34*, 7852–7862. [CrossRef]
19. Craig, E.B.; Sean, B. Modeling and friction estimation for automotive steering torque at very low speeds. *Veh. Syst. Dyn.* **2021**, *59*, 458–484.
20. Bart, F.; Frank, N.; Wim, D. Broadband load torque estimation in mechatronic powertrains using nonlinear Kalman filtering. *IEEE Trans. Ind. Electron.* **2018**, *65*, 2378–2387.
21. Jia, Z.W.; Zhang, Q.H.; Wang, D. A sensorless control algorithm for the circular winding brushless DC motor based on phased voltages and DC current detection. *IEEE Trans. Ind. Electron.* **2021**, *68*, 9174–9184. [CrossRef]
22. Lee, Y.O.; Son, Y.S.; Chung, C.C. Clamping force control for an electric parking brake system: Switched system approach. *IEEE Trans. Veh. Technol.* **2013**, *62*, 2937–2948. [CrossRef]
23. Lee, Y.O.; Jang, M.; Lee, W.; Lee, C.W.; Chung, C.C.; Son, Y.S. Novel clamping force control for electric parking brake systems. *Mechatronics* **2021**, *21*, 1156–1162. [CrossRef]
24. Giseo, P.; Seibum, B.C. Clamping force control based on dynamic model estimation for electromechanical brakes. *Inst. Mech. Eng. Part D J. Automob. Eng.* **2018**, *232*, 2000–2013.
25. Li, Y.J.; Shim, T.; Shin, D.H.; Lee, S.H.; Jin, S.H. Control system design for electromechanical brake system using novel clamping force model and estimator. *IEEE Trans. Veh. Technol.* **2021**, *70*, 8653–8668. [CrossRef]
26. Ding, N.G.; Saied, T. An adaptive integrated algorithm for active front steering and direct yaw moment based on direct Lyapunov method. *Veh. Syst. Dyn.* **2010**, *48*, 1193–1213. [CrossRef]
27. Pacejka, H.B. *Tyre and Vehicle Dynamics*; Butterworth-Heinemann: Oxford, UK, 2002.
28. Ding, N.G. *Method and Application of Parameter Estimation for Automotive Active Control*; Beihang University Press: Beijing, China, 2013. (In Chinese)
29. Tustin, A. The effects of backlash and of speed-dependent friction on the stability of closed-cycle control system. *J. Inst. Electr. Eng.* **1947**, *94*, 143–151. [CrossRef]
30. Li, X.L.; Xue, Z.W.; Yan, X.Y.; Zhang, L.X.; Ma, W.Z.; Hua, W. Low-Complexity Multivector-Based Model Predictive Torque Control for PMSM With Voltage Preselection. *IEEE Trans. Power Electron.* **2021**, *36*, 11726–11738. [CrossRef]
31. Ji, X.W.; He, X.K.; Lv, C.; Liu, Y.H.; Wu, J. A vehicle stability control strategy with adaptive neural network sliding mode theory based on system uncertainty approximation. *Veh. Syst. Dyn.* **2018**, *56*, 923–946. [CrossRef]
32. Yong, J.W.; Gao, F.; Ding, N.G.; He, Y.P. Design and validation of an electro-hydraulic brake system using hardware-in-the-loop real-time simulation. *Int. J. Automot. Technol.* **2017**, *18*, 603–612. [CrossRef]

Disclaimer/Publisher's Note: The statements, opinions and data contained in all publications are solely those of the individual author(s) and contributor(s) and not of MDPI and/or the editor(s). MDPI and/or the editor(s) disclaim responsibility for any injury to people or property resulting from any ideas, methods, instructions or products referred to in the content.